

## Cuboid drop: A low-dimensional model of drop dynamics on a substrate

Tristan Gilet <sup>\*</sup>

*Microfluidics Lab, Department of Aerospace and Mechanical Engineering,  
University of Liège and Allée de la Découverte, 9, 4000 Liège, Belgium*



(Received 24 December 2023; accepted 29 February 2024; published 1 April 2024)

Liquid drops placed on substrates may vibrate, slide, take history-dependent shapes, and even detach or break up when subjected to external forces. Although CFD tools can nowadays reproduce these motions, they are affordable for at most a few drops at a time. This work provides a low-dimensional model of such drops, in which the drop shape is approximated by a rectangular cuboid. The model results in three ordinary differential equations per drop. It is sufficiently simple to allow closed-form solutions in a variety of configurations. By systematically comparing the cuboid predictions to experimental, numerical, and theoretical results previously obtained with real drops, we discuss the extent to which the cuboid approximation reproduces the order of magnitude and qualitative dependence on parameters of a series of phenomena. The latter include natural drop vibrations, the detachment of pendant drops, multiple drop shapes allowed by contact angle hysteresis, the nonlinear retraction of drops after spreading, the sliding or climbing of drops on inclined substrates, and drop-induced damping of substrate vibrations. The cuboid model therefore provides a low-cost representation of drop motion on a substrate in response to arbitrarily complex external forcing.

DOI: [10.1103/PhysRevFluids.9.043601](https://doi.org/10.1103/PhysRevFluids.9.043601)

### I. INTRODUCTION

Raindrops may impact partially wetting surfaces, such as young plant leaves [1–4] or glass windows [5,6]. Subsequently, these surfaces may be covered with sessile water drops of various sizes (Fig. 1). The surfaces often exhibit significant contact angle hysteresis, so the shape of these drops is not uniquely determined; they may be strongly distorted [7] in a way that depends on their history [8]. The drops may vibrate, slide on the substrate, or even fragment in response to various forces, including gravity on an inclined surface [9], wind [5], or mechanical vibrations of the underlying substrate [10,11]. As they move, they may merge with others and form larger clusters with complex shapes that will respond differently to external forces [9]. The overall dynamics of these raindrop residues is complex.

The shape of sessile drops were modeled with various approaches, including geometrical approximations [12–14] or surface energy minimization [15]. Numerical simulations of drop sliding were made with various strategies, including with volumes of fluid [16] or through a lubrication approximation for thin films [17]. These approaches involve the numerical resolution of nonlinear partial differential equations on a mesh much finer than the drop size. They are appropriate to reproduce the unsteady motion and interactions of a few drops. However, using them to model hundreds of such interacting drops (as in Nezlabin *et al.* [9]) would be very demanding in terms of numerical resources. Inferring the statistical behavior of, e.g., raindrop residues on a plant leaf, would require running hundreds of such simulations and is likely out of reach. Alternatively,

---

\*Tristan.Gilet@uliege.be



FIG. 1. (Left and center) Sessile raindrop residues on the aerial parts of plants: leaf blade of *Acer palmatum* (left), and flower petals of *Senecio speciosus* Willd. (center). (Right) A sessile drop is modeled by a rectangular cuboid of length  $\ell$ , width  $w$ , and height  $h$ , placed on a solid substrate. The face on the substrate is centered in  $(x, y, z) = (x_G, 0, 0)$ . Positions  $x = A$  and  $x = B$  correspond to the left and right boundaries of the cuboid drop. Inertial forces corresponding to accelerations  $a_x$  (along  $x$ ) and  $a_z$  (along  $z$ ) are applied at the center of mass of the cuboid.

low-dimensional approaches of drop dynamics model each drop with a mass connected to one or a few linear springs [18–21]. These low-dimensional models were checked to capture the dependence to parameters, at least qualitatively and in the few drop configurations for which they were designed. As they only require to solve a few ordinary differential equations per drop, they may be appropriate for the statistical investigation of the interactions of a large number of drops with a moving substrate.

In this paper, we investigate a low-dimensional model of drop dynamics on solid surfaces, in which the drop is approximated by a rectangular cuboid (Fig. 1). This simple shape is described with only two independent variables (length and width, once the volume is fixed) and allows an immediate analytic evaluation of the potential energy associated to both interfaces and external forces. Moreover, the internal flows can be modeled in such a way that analytic expressions for both the kinetic energy and the viscous dissipation are available. Consequently, the drop dynamics can be obtained by solving the corresponding Lagrange equations. A similar approach was considered by Molacek and Bush [22]: the drop shape was decomposed in spherical harmonics, but the interaction with a solid substrate was not considered. In the present work, with only two shape variables, the rectangular cuboid approximation does only capture two deformation modes and it does not include drop rocking [19,23]. More modes could be added by considering less regular cuboids, with more degrees of freedom. However, the flows therein would be harder to model, and less results would be available in a closed form. The model is described in Sec. II. In Sec. III, it is benchmarked in several configurations, from static drop shapes to natural vibrations and dynamics on moving substrates.

## II. THEORETICAL MODEL

All the variables used in this work are listed in Table I. A sessile liquid drop of constant volume  $\Omega$  is considered, as represented in Fig. 1. Every length of the model is systematically normalized by  $\Omega^{1/3}$  and every time is normalized by  $\sqrt{\rho\Omega/\sigma}$ , where  $\rho$  and  $\sigma$  are the density and surface tension of the liquid, respectively. Consequently, speed, acceleration, force, energy, and power are normalized by  $\sigma^{1/2}\rho^{-1/2}\Omega^{-1/6}$ ,  $\sigma\rho^{-1}\Omega^{-2/3}$ ,  $\sigma\Omega^{1/3}$ ,  $\sigma\Omega^{2/3}$ , and  $\sigma^{3/2}\rho^{-1/2}\Omega^{1/6}$ , respectively. The model assumes a laminar flow inside a drop that does not break up, namely, a flow in which inertia does not dominate other forces. Therefore, it is restricted to a Weber number  $\rho\Omega^{1/3}V^2/\sigma \lesssim 10$  and a Reynolds number  $\rho\Omega^{1/3}V/\mu \lesssim 100$ , where  $V$  is a characteristic speed of the flow inside the drop and  $\mu$  is the dynamical viscosity of the liquid. These upper bounds are only orders of magnitude above which inertial instabilities and liquid breakup are regularly encountered.

TABLE I. List of variables.

$A, B$	Contact line positions	$\beta$	Oscillation decay rate
$a_s$	Forced substrate acceleration	$\tilde{\beta}$	$\beta/\omega$
$C_j, D_j, E_j$	Coefficients	$\gamma$	Surface energy ratio
$F$	Shear function	$\zeta$	Force per unit length at contact line
$f$	Dimensional substrate frequency	$\eta, \xi$	Perturbations of $\ell, w$
$g$	Acceleration of gravity	$\theta$	Young's contact angle
$h$	Cuboid height	$\theta_a, \theta_r$	Advancing, receding contact angles
$I_j$	Flow integrals	$\kappa$	Substrate stiffness/surface tension
$j, m, n$	Integer indices	$\tilde{\kappa}$	Normalized $\kappa$
$\ell$	Cuboid length	$\Lambda$	Slip length
$\ell_e$	Cuboid length at equilibrium	$\lambda$	Lagrange multiplier
$p, q$	Lagrange coordinates	$\mu$	Dynamic viscosity
$s$	Laplace variable	$\rho$	Density
$t$	Time	$\sigma$	Surface tension
$w$	Cuboid width	$\chi$	Substrate mass/drop mass
$x, y, z$	Cartesian coordinates	$\Psi$	Contact line dissipation
$x_G$	$x$ -position of cuboid center of mass	$\Omega$	Cuboid volume
$Z$	Substrate vertical position	$\omega$	Oscillation frequency
$\tilde{z}$	$z/h$	$\omega_s$	Forced substrate frequency
Index b	At bifurcation	$\mathbf{e}_x, \mathbf{e}_y, \mathbf{e}_z$	Unit vectors in cartesian directions
Index i	At initial time	$\mathbf{u}, u_x, u_y, u_z$	Fluid velocity
$\text{Bo}_x, \text{Bo}_z$	Bond numbers (external forces)	$\mathcal{D}$	Dissipation function
Ca	Capillary number	$\mathcal{E}$	Potential energy
Oh	Ohnesorge number	$\mathcal{K}$	Kinetic energy
$\tilde{\text{Oh}}$	Normalized Oh	$\mathcal{L}$	Lagrangian

Axes  $x$  and  $y$  are in the plane of the substrate, while the axis  $z$  is perpendicular to the substrate (with  $z = 0$  on the substrate). The drop is on the side of the substrate corresponding to  $z > 0$ . The drop is approximated by a rectangular cuboid of dimensionless length  $\ell$  along  $x$ , width  $w$  along  $y$ , and height  $h$  along  $z$ . Volume conservation implies  $\ell wh = 1$  at any time. The center of mass of this cuboid drop is in  $(x, y, z) = (x_G, 0, h/2)$ . The contact lines (cuboid boundaries on the substrate) are in  $x = x_G \pm \ell/2$  and  $y = \pm w/2$ .

### A. Potential energy

The potential energy comprises the surface energy associated to interfaces and the energy associated to conservative external forces. We define the surface energy ratio

$$\gamma = \frac{\sigma_{\text{SG}} - \sigma_{\text{SL}}}{\sigma}, \quad (1)$$

where  $\sigma_{\text{SG}}$  and  $\sigma_{\text{SL}}$  represent the energy per unit area associated to solid-gas and solid-liquid interfaces, respectively. The cuboid drop is subjected to inertial forces resulting from accelerations  $a_x$  and  $a_z$ , along  $x$  and  $z$ , respectively. These accelerations include the components of gravity. Once normalized by  $\sigma \rho^{-1} \Omega^{-2/3}$ , they correspond to Bond numbers

$$\text{Bo}_x = \frac{\rho a_x \Omega^{2/3}}{\sigma} \quad \text{and} \quad \text{Bo}_z = \frac{\rho a_z \Omega^{2/3}}{\sigma}. \quad (2)$$

The potential energy, normalized by  $\sigma \Omega^{2/3}$ , is then

$$\mathcal{E} = \frac{2}{\ell} + \frac{2}{w} + (1 - \gamma)\ell w - \text{Bo}_x x_G - \frac{\text{Bo}_z}{2\ell w}, \quad (3)$$

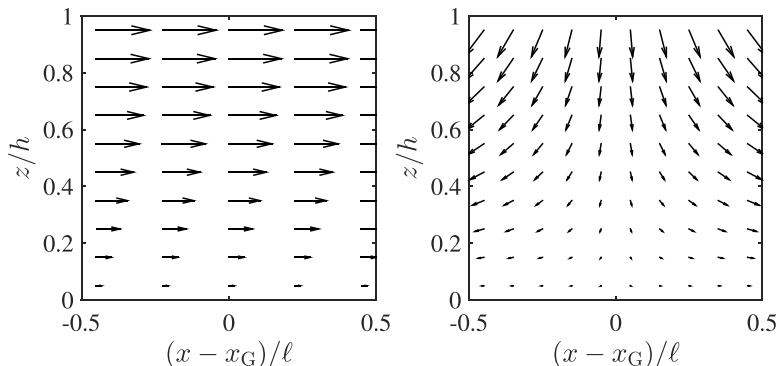


FIG. 2. Velocity profile  $\mathbf{u}$  inside the cuboid drop, as a function of normalized coordinates  $(x - x_G)/\ell \in [-0.5, 0.5]$  and  $z/h \in [0, 1]$ , according to Eqs. (4) and (19). The left graph corresponds to the translation of the cuboid drop (shear flow), while the right graph corresponds to the flattening of the cuboid drop (stagnation point flow). The general velocity field inside the cuboid includes a linear combination of both shear flow and stagnation point flow. In both graphs, the function  $F$  corresponds to Eq. (19).

where the first two terms represent the surface energy of the liquid-air interface and the third term represents the surface energy of the solid-liquid interface.

As explained in many textbooks (e.g., Sec. 2.1.4 in Myshkis *et al.* [24]), the Young-Laplace law, that relates the local discontinuity of normal stress at the liquid-air interface to the local mean curvature, is directly derived from the minimization of the potential energy associated to the interface shape. The cuboid approximation is a strong constraint on the interface shape that may seem unrealistic. Indeed, the mean curvature (and corresponding pressure jump across the interface) is uniformly zero on the flat sides of the cuboid, and it is infinite at the cuboid corners. Nevertheless, we will show that minimizing the potential energy under this cuboid constraint yields a shape with an aspect ratio that is close to that of real drop shapes.

### B. Flow pattern and kinetic energy

To predict the cuboid drop dynamics, we need to estimate how much kinetic energy corresponds to the flows generated by the cuboid drop motion and vibration. Solving the full 3D unsteady Navier-Stokes equations does not seem possible analytically, even for a cuboid liquid shape. Therefore, we aim at building an *ad hoc* flow velocity profile  $\mathbf{u}(x, y, z, t) = u_x \mathbf{e}_x + u_y \mathbf{e}_y + u_z \mathbf{e}_z$  that satisfies at least the continuity equation ( $\nabla \cdot \mathbf{u} = 0$ , as the flow is assumed incompressible) and approximates some expected flow patterns. More specifically, we assume that the liquid inside the cuboid drop experiences a stagnation-point flow associated to changes of dimensions (proportional to  $\dot{\ell}$  or  $\dot{w}$ ) and a translation associated to sliding in the  $x$  direction (proportional to  $\dot{x}_G$ ). Including some translation and corresponding shear flow in the  $y$  direction would be straightforward. The corresponding velocity field is a linear combination of shear flow and stagnation-point flow, namely,

$$u_x = \left[ \dot{x}_G + \frac{\dot{\ell}}{\ell}(x - x_G) \right] \frac{dF}{d\tilde{z}}, \quad u_y = \frac{\dot{w}}{w} y \frac{dF}{d\tilde{z}}, \quad u_z = - \left( \frac{\dot{\ell}}{\ell} + \frac{\dot{w}}{w} \right) h F(\tilde{z}), \quad (4)$$

where  $F(\tilde{z})$  is a function of  $\tilde{z} = z/h$  that results from the shear induced by the substrate (no-slip condition). The shear and stagnation-point contributions to the velocity profile of equation (4) are represented in Fig. 2. Flow recirculation, as observed, e.g., in rolling drops on superhydrophobic substrates [25] is here neglected.

The no-slip boundary condition on the solid substrate yields

$$\lim_{z \rightarrow 0} \mathbf{u} = \mathbf{0} \Rightarrow \lim_{\tilde{z} \rightarrow 0} \frac{dF}{d\tilde{z}} = 0. \quad (5)$$

The no-shear boundary condition at the free surface in  $z = h$  yields

$$\lim_{z \rightarrow h} \frac{\partial u_x}{\partial z} = \lim_{z \rightarrow h} \frac{\partial u_y}{\partial z} = 0 \Rightarrow \lim_{\tilde{z} \rightarrow 1} \frac{d^2 F}{d\tilde{z}^2} = 0. \quad (6)$$

The kinematic condition at this free surface yields

$$\lim_{z \rightarrow h} u_z = \dot{h} \Rightarrow F(1) = 1. \quad (7)$$

The boundary condition on the lateral faces of the cuboid drop should ideally be

$$\lim_{x \rightarrow x_G \pm \ell/2} u_x = \dot{x}_G \pm \frac{\dot{\ell}}{2}, \quad \lim_{y \rightarrow \pm w/2} u_y = \pm \frac{\dot{w}}{2}. \quad (8)$$

However, owing to the presence of shear, the velocity field of Eq. (4) cannot exactly satisfy these boundary conditions. For a real drop, there should be some additional flow in the  $z$  direction that redistributes the fluid around the lateral boundaries. Modeling these flows intimately associated to contact line dynamics is still very challenging [26] and beyond the scope of this work. Nevertheless, the condition  $F(1) = 1$  ensures that the boundary conditions on the lateral faces are satisfied on average over  $z$ , namely,

$$\lim_{x \rightarrow x_G \pm \ell/2} \frac{1}{h} \int_0^h u_x dz = \dot{x}_G \pm \frac{\dot{\ell}}{2}, \quad \lim_{y \rightarrow \pm w/2} \frac{1}{h} \int_0^h u_y dz = \pm \frac{\dot{w}}{2}. \quad (9)$$

There is no need for a local dynamic boundary condition associated to the normal stress discontinuity across the liquid-air interface. Indeed, the local stress and its influence on the velocity field through the Navier-Stokes equations are not considered here. By ensuring a global balance of momentum at the cuboid scale, the Lagrange equations will effectively replace this dynamic condition. The model may also be extended to include pressure and shear stress that would be applied to the drop boundaries (e.g., from some wind pushing and shearing the droplet). The surface integral of the pressure would be taken into account as a contribution to  $\text{Bo}_x$  and  $\text{Bo}_z$  (this is valid provided that the drop motion does not significantly modify this pressure in return), while the shear stress would be included directly in Eq. (6).

The kinetic energy associated to this flow, again normalized by  $\sigma \Omega^{2/3}$ , is

$$\mathcal{K} = \int_{x_G - \ell/2}^{x_G + \ell/2} dx \int_{-w/2}^{w/2} dy \int_0^h \frac{\mathbf{u} \cdot \mathbf{u}}{2} dz = \frac{I_1}{2} \left( \dot{x}_G^2 + \frac{\dot{\ell}^2 + \dot{w}^2}{12} \right) + \frac{I_2}{2\ell^2 w^2} \left( \frac{\dot{\ell}}{\ell} + \frac{\dot{w}}{w} \right)^2, \quad (10)$$

with

$$I_1 = \int_0^1 \left( \frac{dF}{d\tilde{z}} \right)^2 d\tilde{z}, \quad I_2 = \int_0^1 F^2 d\tilde{z}. \quad (11)$$

### C. Viscous dissipation

The viscous dissipation in a drop comprises a contribution from the shear in the bulk, and another contribution from the shear at the moving contact line [27,28]. The dissipated power in the bulk,

normalized by  $\sigma^{3/2}\rho^{-1/2}\Omega^{1/6}$ , is given by

$$\begin{aligned} \mathcal{D}_{\text{bulk}} &= \text{Oh} \int_{x_G-\ell/2}^{x_G+\ell/2} dx \int_{-w/2}^{w/2} dy \int_0^h dz \\ &\quad \cdot \left[ 2 \left( \frac{\partial u_x}{\partial x} \right)^2 + 2 \left( \frac{\partial u_y}{\partial y} \right)^2 + 2 \left( \frac{\partial u_z}{\partial z} \right)^2 + \left( \frac{\partial u_x}{\partial z} \right)^2 + \left( \frac{\partial u_y}{\partial z} \right)^2 \right] \\ &= \text{Oh} \left[ 4I_1 \left( \frac{\ell^2}{\ell^2} + \frac{\dot{w}^2}{w^2} + \frac{\dot{\ell}\dot{w}}{\ell w} \right) + I_3 \ell^2 w^2 \left( \dot{x}_G^2 + \frac{\ell^2 + \dot{w}^2}{12} \right) \right], \end{aligned} \quad (12)$$

where

$$I_3 = \int_0^1 \left( \frac{d^2 F}{d\tilde{z}^2} \right)^2 d\tilde{z}, \quad (13)$$

and where  $\text{Oh} = \mu/\sqrt{\rho\sigma\Omega^{1/3}}$  is the Ohnesorge number. Velocity derivatives that are identically zero are not explicitly written in Eq. (12). The dissipation at the contact line depends on a characteristic slip length  $\Lambda \sim 10$  nm at which the contact line singularity is resolved [29]. It is here modeled in a way similar to Huh and Scriven [27], Kim *et al.* [29]:

$$\mathcal{D}_{\text{CL}} = \text{Oh}\Psi(\theta) \frac{4w\dot{x}_G^2 + w\dot{\ell}^2 + \ell\dot{w}^2}{4}, \quad (14)$$

where  $\theta$  is the contact angle and

$$\Psi(\theta) = \frac{\sin^2 \theta}{\theta - \sin \theta \cos \theta} \ln \left( \frac{\Omega^{1/3}}{\Lambda} \right). \quad (15)$$

Millimeter-sized drops are considered in this work, for which  $\Omega^{1/3} \sim 10^5 \Lambda$ . Therefore, it is assumed that

$$\ln \left( \frac{\Omega^{1/3}}{\Lambda} \right) = 11.5.$$

Changing either  $\Lambda$  or  $\Omega^{1/3}$  by a factor of 10 would only change  $\Psi$  by 20%. The total dissipation is

$$\mathcal{D} = \mathcal{D}_{\text{bulk}} + \mathcal{D}_{\text{CL}}. \quad (16)$$

#### D. Shear function $F(\tilde{z})$

We propose a polynomial shear function that satisfies the boundary conditions (5) to (7):

$$F(\tilde{z}) = 1 - \frac{n}{n-1}(1-\tilde{z}) + \frac{(1-\tilde{z})^n}{n-1}, \quad (17)$$

with  $n \in \mathbb{N}$ ,  $n \geq 3$ . It also satisfies

$$\lim_{\tilde{z} \rightarrow 1} \frac{d^{(m)} F}{d\tilde{z}^{(m)}} = 0, \quad m \in [2, n-1].$$

Higher values of  $n$  yield more uniform velocity profiles around  $z = h$ , and consequently more shear at the wall in  $z = 0$ . The integrals involved in Eqs. (11) and (13) are

$$I_1 = \frac{2n}{2n-1}, \quad I_2 = \frac{n^2(2n+5)}{3(n+1)(n+2)(2n+1)}, \quad I_3 = \frac{n^2}{2n-3}. \quad (18)$$

The case  $n = 3$ , which is considered in the remainder of this work, corresponds to the simplest polynomial that satisfies all boundary conditions,

$$F(\bar{z}) = \frac{\bar{z}^2}{2}(3 - \bar{z}). \quad (19)$$

It yields  $I_1 = 6/5$ ,  $I_2 = 33/140$ , and  $I_3 = 3$ . Another, more realistic, choice for  $F(\bar{z})$  could be the function describing a Hiemenz flow (stagnation-point flow with boundary layer). This flow profile would satisfy the Navier-Stokes equations, at the condition that the flow is steady (i.e.,  $\partial_t u_x = \partial_t u_y = \partial_t u_z = 0$ ). However,  $F$  would have to be calculated by solving an ordinary differential equation and analytic solutions could not be sought anymore.

### E. Lagrange equations

The Lagrangian  $\mathcal{L} = \mathcal{K} - \mathcal{E}$  is a function of the generalized coordinates  $(x_G, \ell, w)$  and their time derivatives. The possible pinning of contact lines translates into constraints on these coordinates, that are expressed more easily if the generalized coordinates actually correspond to the position of the contact lines. Therefore, we prefer the generalized coordinates  $q_j = (A, B, w)$ , where  $A = x_G - \ell/2$  and  $B = x_G + \ell/2$  correspond to the positions of the left and right contact lines along the  $x$  axis, respectively.

Lagrange's equations are

$$\frac{d}{dt} \left( \frac{\partial \mathcal{L}}{\partial \dot{q}_j} \right) = \frac{\partial \mathcal{L}}{\partial q_j} - \frac{\partial \mathcal{D}}{\partial \dot{q}_j} - \lambda_j p_j, \quad (20)$$

where  $p_j = (w, w, \ell)$ , is the length of the contact line associated to  $q_j$ , and  $\lambda_j$  is the force per unit length exerted at that contact line (counted positive in the direction of decreasing  $q_j$ ), owing to contact angle hysteresis. The Lagrange equations ensure that momentum variations at the drop scale obey Newton's second law, even though the chosen velocity profile does not satisfy local momentum balance (Navier-Stokes equations). Each Lagrange equation must be customized, depending if the corresponding contact lines are pinned or not. When the contact lines associated to  $q_j$  are pinned,  $\lambda_j$  is adapted to guarantee that  $\dot{q}_j = \ddot{q}_j = 0$ . When these contact lines move,  $\lambda_j = \zeta \text{sign}(\dot{q}_j)$ , where  $\zeta > 0$  is the magnitude of the force per unit length exerted by the moving contact line. The customized equations (20) can be integrated in time until any contact line changes regime (between pinned, advancing and receding). Then equations (20) must be customized again according to the new contact line conditions.

To illustrate this, we consider the example of a pinned contact line in  $x = B$ , an advancing contact line in  $x = A$  (i.e.,  $\dot{A} < 0$ ) and advancing contact lines in  $y = \pm w/2$  (i.e.,  $\dot{w} > 0$ ). The equations to be solved are then

$$\begin{aligned} \begin{bmatrix} \ddot{A} \\ \ddot{w} \end{bmatrix} &= \begin{bmatrix} \frac{\partial^2 \mathcal{L}}{\partial A^2} & \frac{\partial^2 \mathcal{L}}{\partial A \partial w} \\ \frac{\partial^2 \mathcal{L}}{\partial A \partial w} & \frac{\partial^2 \mathcal{L}}{\partial w^2} \end{bmatrix}^{-1} \left( \begin{bmatrix} \frac{\partial \mathcal{L}}{\partial A} - \frac{\partial \mathcal{D}}{\partial A} + \zeta w \\ \frac{\partial \mathcal{L}}{\partial w} - \frac{\partial \mathcal{D}}{\partial w} - \zeta \ell \end{bmatrix} - \begin{bmatrix} \frac{\partial^2 \mathcal{L}}{\partial A \partial A} & \frac{\partial^2 \mathcal{L}}{\partial w \partial A} \\ \frac{\partial^2 \mathcal{L}}{\partial A \partial w} & \frac{\partial^2 \mathcal{L}}{\partial w \partial w} \end{bmatrix} \begin{bmatrix} \dot{A} \\ \dot{w} \end{bmatrix} \right), \\ \lambda_B &= \frac{1}{w} \left( \frac{\partial \mathcal{L}}{\partial B} - \frac{\partial \mathcal{D}}{\partial B} - \begin{bmatrix} \frac{\partial^2 \mathcal{L}}{\partial A \partial B} & \frac{\partial^2 \mathcal{L}}{\partial w \partial B} \end{bmatrix} \begin{bmatrix} \dot{A} \\ \dot{w} \end{bmatrix} - \begin{bmatrix} \frac{\partial^2 \mathcal{L}}{\partial A \partial B} & \frac{\partial^2 \mathcal{L}}{\partial w \partial B} \end{bmatrix} \begin{bmatrix} \dot{A} \\ \dot{w} \end{bmatrix} \right), \end{aligned} \quad (21)$$

with  $\dot{B} = \ddot{B} = 0$ . These equations can be integrated in time until any contact line changes regime. The contact line in  $x = B$  will remain pinned as long as  $|\lambda_B| < \zeta$  and unpinning will occur when  $|\lambda_B| \rightarrow \zeta$ . Contact lines in  $x = A$  and  $y = \pm w/2$  will possibly become pinned as soon as they stop, i.e., as soon as  $\dot{A} \rightarrow 0$  or  $\dot{w} \rightarrow 0$ , respectively.

### F. Numerical implementation

The Lagrange equations (20) were solved in Matlab. First, the functions of  $(A, B, w)$  involved in these equations were calculated symbolically. Then the resulting Lagrange equations were solved

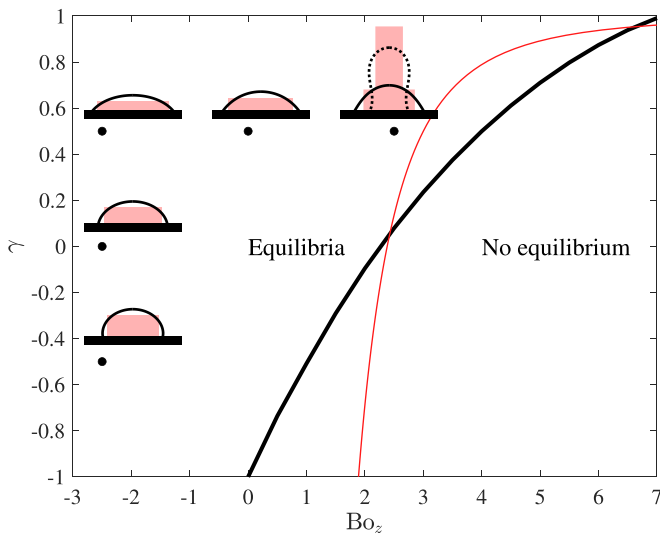


FIG. 3. Region of existence of equilibrium positions in a  $(Bo_z, \gamma)$  diagram. The curves represent the maximal Bond number  $Bo_{zb}$  beyond which no equilibrium can be found, for the cuboid drop (thin red line) and for an axisymmetric drop (solution of Young-Laplace equation—thick black line). The shape of the liquid interface is represented for five points (black dots) corresponding to different pairs  $(Bo, \gamma)$ , for the cuboid drop (light red boxes) and for the axisymmetric drop (black lines). The solid (respectively, dotted) lines correspond to stable (respectively, unstable) solutions of the Young-Laplace equation.

numerically, thanks to the function `ode45` and the associated event detection tool. The script is given in Supplemental Material [30].

### III. TEST CASES

In the remainder of this work, several test cases are considered to compare the predictions of the cuboid drop to either experimental or theoretical results obtained for real drops.

#### A. Static cuboid drop, $Bo_x = 0, \zeta = 0$

The first considered equilibrium case is a static cuboid drop ( $\dot{x}_G = \dot{\ell} = \dot{w} = 0$ ), only submitted to external forces normal to the substrate ( $Bo_x = 0$ ) and without any contact angle hysteresis ( $\zeta = 0$ ). At equilibrium, the Lagrange equations reduce to  $\partial\mathcal{E}/\partial\ell = \partial\mathcal{E}/\partial w = 0$ . Since  $\mathcal{E}$  is symmetric, the equilibrium solutions must satisfy  $(\ell, w) = (\ell_e, \ell_e)$ , where  $\ell_e$  is a positive root of the fourth-order polynomial

$$P(\ell) \equiv 2(1 - \gamma)\ell^4 - 4\ell + Bo_z, \quad P(\ell_e) = 0. \quad (22)$$

This polynomial  $P(\ell)$  has only one minimum, in

$$\ell_b \equiv [2(1 - \gamma)]^{-1/3} > 0. \quad (23)$$

Consequently, equilibrium solutions can only be found when

$$Bo_z < Bo_{zb} \equiv \frac{3}{[2(1 - \gamma)]^{1/3}}. \quad (24)$$

The Bond number  $Bo_{zb}$  corresponds to a saddle-node bifurcation. As it physically represents the moment where inertial forces outbalance capillary forces, it may be seen as the analog of some Rayleigh-Taylor instability threshold. It is represented in Fig. 3 as a curve that delimits the region of

existence of equilibrium solutions in the two-dimensional diagram  $(Bo_z, \gamma)$ . In the same figure, the equilibrium shapes of the cuboid drops are shown for different pairs  $(Bo_z, \gamma)$ . They are compared to the solutions of the axisymmetric Young-Laplace equation, which correspond to the shapes of the liquid interface that exactly minimizes the free energy (cf. Supplemental Material [30]). The cuboid approximation is relatively close to the exact interface shape, and its aspect ratio varies consistently with either  $\gamma$  or  $Bo_z$ . The bifurcation curve associated to the Young-Laplace equation is qualitatively similar to that of the cuboid drops: in both cases,  $Bo_{zb}$  is a monotonically increasing function of  $\gamma$  that is close to  $Bo_{zb} \simeq 2.3$  for  $\gamma = 0$ , and equilibrium shapes can only be found for  $Bo_z < Bo_{zb}$ . However, the cuboid approximation provides solutions to drops accelerated away from a hydrophobic substrate ( $Bo_z > 0, \gamma < 0$ ) while the Young-Laplace equation does not always have some. Real drops in the same conditions (e.g., pendant drops) would simply detach from the substrate. Conversely, the maximum  $Bo_z$  at which equilibria can be found for drops accelerated away from a hydrophilic substrate is significantly underestimated by the cuboid approximation. Finally, the cuboid approximation predicts an unphysical divergence of  $Bo_{zb}$  at  $\gamma \rightarrow 1$ .

In the particular case of  $Bo_z = 0$  (no acceleration), the equilibrium solution of the cuboid drop is given by

$$\ell_e = \ell_0 \equiv \left[ \frac{2}{1 - \gamma} \right]^{1/3}. \quad (25)$$

The analog of contact angle for a cuboid drop is therefore

$$\cos \theta = \gamma = 1 - \frac{2}{\ell_e^3}. \quad (26)$$

The corresponding aspect ratio is

$$\frac{h}{\ell} = \frac{1 - \gamma}{2}. \quad (27)$$

This function is very close to the aspect ratio of a real drop, which in similar conditions would be shaped as a spherical cap (cf. Supplemental Material [30]).

Normalizing Eq. (22) by  $4\ell_0$  yields

$$\frac{Bo_z}{4\ell_0} = \frac{\ell_e}{\ell_0} - \left( \frac{\ell_e}{\ell_0} \right)^4. \quad (28)$$

This polynomial relation between  $\ell_e/\ell_0$  and  $Bo_z/(4\ell_0)$  is represented in Fig. 4, together with the similarly normalized solutions of the Young-Laplace equation (assuming that  $\ell$  is equivalent to the diameter at the drop basis, cf. Supplemental Material [30]). The equilibrium curve of the cuboid drop described by Eq. (28) is remarkably close to the envelope of the Young-Laplace solutions.

### B. Cuboid drop stability and vibrations, $Bo_x = 0, \zeta = 0$

The linear stability of the aforementioned equilibria can be inferred from perturbations  $\ell = \ell_e(1 + \eta)$ ,  $w = \ell_e(1 + \xi)$ , with  $|\eta| \ll 1$  and  $|\xi| \ll 1$  [31]. The linearized Lagrange equations are

$$\begin{bmatrix} C_1 & C_2 \\ C_2 & C_1 \end{bmatrix} \begin{bmatrix} \ddot{\eta} \\ \ddot{\xi} \end{bmatrix} + \text{Oh} \begin{bmatrix} C_3 & C_4 \\ C_4 & C_3 \end{bmatrix} \begin{bmatrix} \dot{\eta} \\ \dot{\xi} \end{bmatrix} + \begin{bmatrix} C_5 & C_6 \\ C_6 & C_5 \end{bmatrix} \begin{bmatrix} \eta \\ \xi \end{bmatrix} = \begin{bmatrix} 0 \\ 0 \end{bmatrix}, \quad (29)$$

with

$$C_1 = \frac{I_1}{12} + \frac{I_2}{\ell_e^6}, \quad C_3 = \frac{8I_1}{\ell_e^2} + \frac{I_3 \ell_e^4}{6} + \frac{\Psi \ell_e}{2}, \quad C_5 = 2(1 - \gamma),$$

$$C_2 = \frac{I_2}{\ell_e^6}, \quad C_4 = \frac{4I_1}{\ell_e^2}, \quad C_6 = 2(1 - \gamma) - \frac{2}{\ell_e^3}.$$

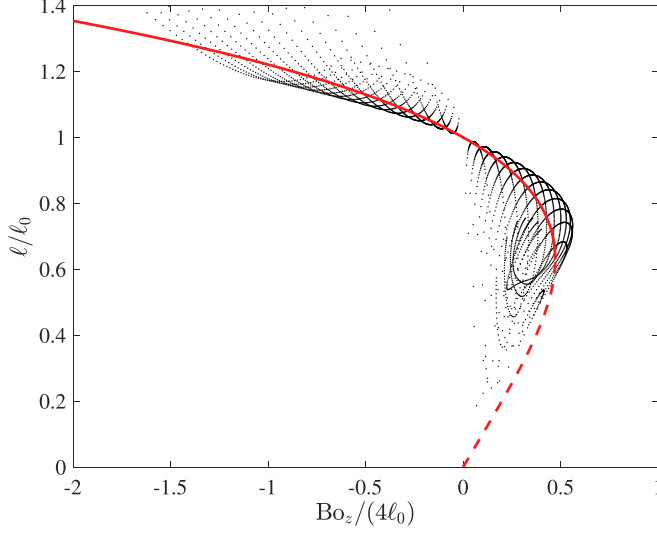


FIG. 4. Equilibrium solutions as a function of the Bond number. The red curve represents the equilibrium length  $\ell = \ell_e$  of the cuboid drop, normalized by the solution  $\ell_0$  obtained at  $\text{Bo}_z = 0$ . The solid (respectively, dashed) part of this curve corresponds to stable (respectively, unstable) solutions. The black dots represent the solutions of the Young-Laplace equation in the full range  $\gamma \in [-1, 1]$ , assuming that the diameter at the drop basis is equivalent to  $\ell$  (cf. Supplemental Material [30]).

These differential equations admit solutions of the form  $\eta = \eta_i e^{st}$  and  $\xi = \xi_i e^{st}$ , where  $s$  is a Laplace variable and  $(\eta_i, \xi_i)$  are the initial perturbation amplitudes. The latter are not identically zero if  $s$  is a complex solution of either

$$(C_1 - C_2)s^2 + \text{Oh}(C_3 - C_4)s + (C_5 - C_6) = 0 \quad (30)$$

or

$$(C_1 + C_2)s^2 + \text{Oh}(C_3 + C_4)s + (C_5 + C_6) = 0. \quad (31)$$

Equation (30) corresponds to antisymmetric perturbations  $\eta = -\xi$ , while Eq. (31) corresponds to symmetric perturbations  $\eta = \xi$ . These vibration modes are illustrated in movies 1 and 2, available in the Supplemental Material [30]. Antisymmetric perturbations are overdamped when the discriminant of Eq. (30) is positive, namely when

$$\text{Oh}^2 > \frac{4(C_1 - C_2)(C_5 - C_6)}{(C_3 - C_4)^2}, \quad (32)$$

and they are underdamped otherwise. In the latter case,  $s = -\beta + i\omega$ , the decay rate is

$$\beta = \text{Oh} \left[ \frac{24}{\ell_e^2} + \frac{I_3}{I_1} \ell_e^4 + \frac{3\Psi \ell_e}{I_1} \right], \quad (33)$$

and the squared natural frequency is

$$\omega^2 = \frac{24}{I_1 \ell_e^3} - \beta^2. \quad (34)$$

In any case, equilibrium solutions are always linearly stable to antisymmetric perturbations. The damping of symmetric perturbations depends on the sign of

$$C_5 + C_6 = 4(1 - \gamma) - \frac{2}{\ell_e^3}. \quad (35)$$

When  $C_5 + C_6 > 0$ , symmetric perturbations are overdamped when

$$\text{Oh}^2 > \frac{4(C_1 + C_2)(C_5 + C_6)}{(C_3 + C_4)^2} \quad (36)$$

and underdamped otherwise. In the latter case,  $s = -\beta + i\omega$ , the decay rate is

$$\beta = \text{Oh} \frac{\frac{12I_1}{\ell_e^2} + \frac{I_3}{6} \ell_e^4 + \frac{\Psi \ell_e}{2}}{\frac{I_1}{12} + \frac{2I_2}{\ell_e^6}}, \quad (37)$$

and the squared natural frequency is

$$\omega^2 = \frac{4(1 - \gamma) - \frac{2}{\ell_e^3}}{\frac{I_1}{12} + \frac{2I_2}{\ell_e^6}} - \beta^2. \quad (38)$$

When  $C_5 + C_6 < 0$ , the discriminant of Eq. (31) is always positive, and one of the real solutions  $s$  is positive, so symmetric perturbations grow exponentially. The equilibrium solutions corresponding to

$$\ell_e^3 < \frac{1}{2(1 - \gamma)} \quad (39)$$

are therefore unstable. The case  $C_5 + C_6 = 0$  corresponds to the previously discussed saddle-node bifurcation. Beyond the bifurcation point, the symmetric perturbation grows exponentially, which yields an infinite cuboid elongation in the direction normal to the substrate. A real drop in similar conditions would break into one or several droplets [32].

The symmetric perturbation is analog to the zonal vibration mode of a sessile drop corresponding to the spherical harmonic  $Y_2^0$  [33]. Similarly, the antisymmetric perturbation is analog to the sectoral vibration mode of a sessile drop corresponding to the spherical harmonic  $Y_2^2$ . However, a sessile drop may exhibit a variety of other vibration modes [34] that, by definition, cannot be captured by the cuboid model. These missed modes include the rocking mode  $Y_2^1$ , as well as modes  $Y_\ell^m$  with  $\ell > 2$ ,  $m \in [-\ell, \ell]$ .

The natural frequencies predicted for the cuboid drop by Eqs. (34) and (38) are compared to the corresponding frequencies for a sessile drop in Figs. 5 and 6. Those sessile drop frequencies are mostly obtained from numerical simulations of an inviscid sessile drop (Zhang *et al.* [35] and previous studies cited therein). We could also find one experimental study [36] that considered sessile drop vibrations with a sufficiently low contact angle hysteresis (and therefore a freely moving contact line) [37]. These experiments were made at  $\gamma \simeq -0.95$  for variable drop volume (i.e., variable  $\text{Bo}_z < 0$ ). In Fig. 5, data from Mettu and Chaudhury [36] are extrapolated to  $\text{Bo}_z \rightarrow 0$ .

The variations of  $\omega$  with  $\gamma$  and  $\text{Bo}_z$  are always qualitatively reproduced by the cuboid model. In particular, Fig. 5 confirms that: (i) the dimensionless frequency of the zonal mode (2,0) increases with  $\gamma$  for  $\gamma \lesssim 0.3$ , experiences a maximum  $\omega \sim 4$  at  $\gamma \sim 0.3$ , and decreases for higher  $\gamma$ , and (ii) the frequency of the sectoral mode monotonically decreases with increasing  $\gamma$ . The experimental data point at  $\gamma \simeq -0.95$  is at mid-way between the extrapolation of the numerical prediction of Zhang *et al.* [35] and the cuboid prediction. Figure 6 indicates that, for  $\text{Bo}_z < 0$ , similarly for the cuboid prediction and the calculation of Zhang *et al.* [35], the frequency of the zonal mode increases with increasing  $|\text{Bo}_z|$  (except for  $\gamma = \sqrt{2}/2$  where Zhang *et al.* [35] predicts a slightly decrease), while those of sectoral modes decrease with increasing  $|\text{Bo}_z|$ . In the particular case of  $\gamma = 0$  and  $\text{Bo}_z = 0$ , a real sessile drop would take the shape of a hemisphere, and the corresponding Rayleigh frequency would be  $\omega = 4\sqrt{\pi/3} \simeq 4.1$  for both modes. For the cuboid drop in the same conditions, the symmetric mode yields  $\omega = \sqrt{840/61} \simeq 3.7$  and the antisymmetric mode yields  $\omega = \sqrt{10} \simeq 3.2$ .

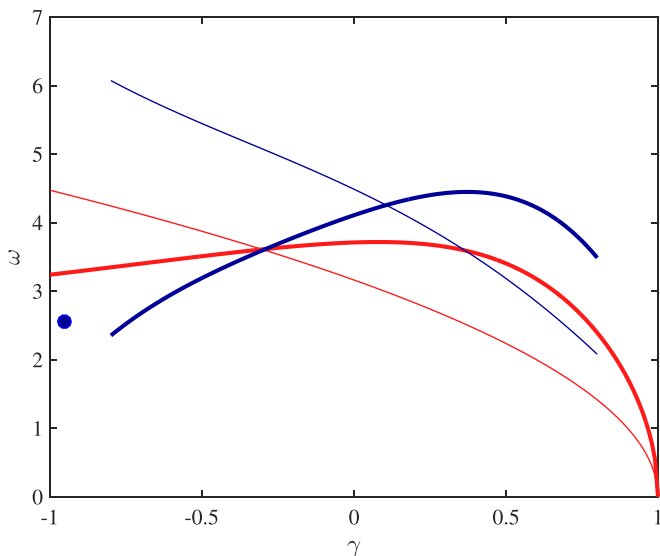


FIG. 5. Variation of the natural frequency  $\omega$  of a sessile drop with  $\gamma$ , for  $Bo_z = 0$ . Red lines correspond to cuboid drops, while dark blue lines correspond to the numerical solution of Zhang *et al.* [35] for real drops. Thick lines represent the zonal (2,0) mode, while thin lines represent the sectoral (2,2) mode. The dark blue dot corresponds to the experimental data from Mettu and Chaudhury [36].

### C. Contact angle hysteresis

Contact angle hysteresis is defined as the difference between the contact angle  $\theta_a$  of advancing contact lines, and the contact angle  $\theta_r$  of receding contact lines. It was here indirectly introduced in

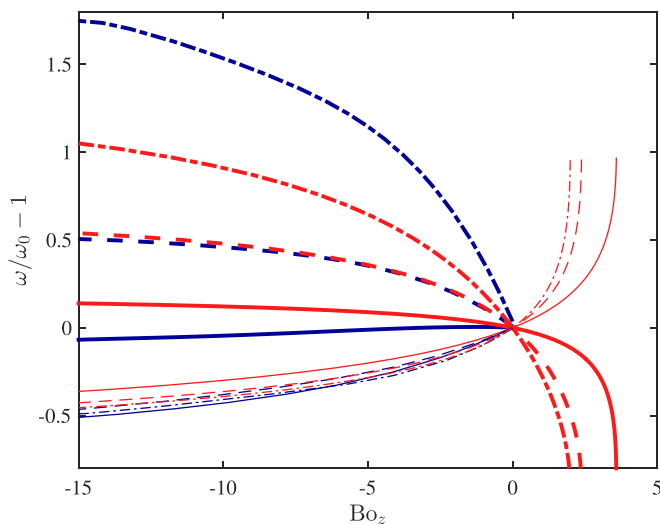


FIG. 6. Variation of the natural frequency  $\omega$  of a sessile drop with the Bond number  $Bo_z$ , relative to the frequency  $\omega_0$  at  $Bo_z = 0$ . Red lines correspond to cuboid drops, while dark blue lines correspond to the numerical solution of Zhang *et al.* [35] for real drops. Thick lines represent the zonal (2,0) mode, while thin lines represent the sectoral (2,2) mode. Solid, dashed, and dash-dotted curves correspond to  $\gamma = \sqrt{2}/2$ ,  $\gamma = 0$  and  $\gamma = -\sqrt{2}/2$ , respectively.

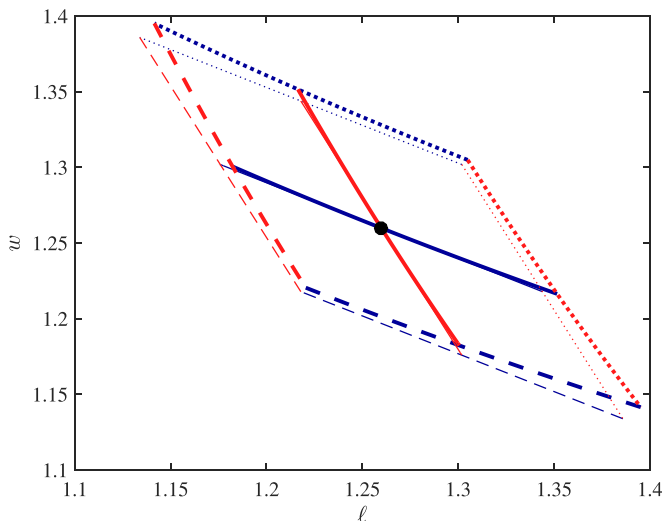


FIG. 7. Region of the phase space  $(\ell, w)$  in which a cuboid drop remains static thanks to contact angle hysteresis, for  $\text{Bo}_z = 0$ ,  $\gamma = 0$  and  $\zeta = 0.1$ . Thick lines are exact solutions of Eq. (40) while thin lines correspond to the approximate solutions (41). The dark blue (respectively, red) lines represent variations of  $\lambda_\ell \in [-\zeta, \zeta]$  (respectively,  $\lambda_w \in [-\zeta, \zeta]$ ). Solid blue (respectively, red) lines correspond to  $\lambda_w = 0$  (respectively,  $\lambda_\ell = 0$ ). Dashed blue (respectively, red) lines correspond to  $\lambda_w = \zeta$  (respectively,  $\lambda_\ell = \zeta$ ). Dotted blue (respectively, red) lines correspond to  $\lambda_w = -\zeta$  (respectively,  $\lambda_\ell = -\zeta$ ).

Lagrange equations (20) thanks to an additional force per unit length  $\lambda$  applied at the contact line. Values of  $\lambda$  in the range  $]-\zeta, \zeta[$  correspond to pinned contact lines, while  $\lambda = \zeta$  (respectively,  $\lambda = -\zeta$ ) corresponds to an advancing (respectively, receding) contact line. The link between  $\zeta$ ,  $\theta_a$  and  $\theta_r$  is established in the Supplemental Material [30] for the case of a drop shaped as a spherical cap. We associate  $\lambda_\ell$  and  $\lambda_w$  to variations of  $\ell$  and  $w$ , respectively. At equilibrium, the Lagrange equations for  $\ell$  and  $w$  are

$$\begin{aligned} \frac{\partial \mathcal{E}}{\partial \ell} = -\lambda_\ell w &\Rightarrow (1 - \gamma + \lambda_\ell) \ell^2 = \frac{4w - \text{Bo}_z}{2w^2}, \\ \frac{\partial \mathcal{E}}{\partial w} = -\lambda_w \ell &\Rightarrow (1 - \gamma + \lambda_w) w^2 = \frac{4\ell - \text{Bo}_z}{2\ell^2}. \end{aligned} \quad (40)$$

Each pair  $(\lambda_\ell, \lambda_w)$  corresponds to a different solution  $(\ell, w)$  of these Lagrange equations, represented in Fig. 7.

Approximate solutions to Eq. (40) can be obtained in the limit  $\zeta \ll 1$ :

$$\begin{aligned} \ell &= \ell_c \left[ 1 + \frac{\ell_c^6 (1 - \gamma) (\lambda_w - \lambda_\ell) - \ell_c^3 \lambda_w}{4\ell_c^3 (1 - \gamma) - 2} + \mathcal{O}(\zeta^2) \right], \\ w &= \ell_c \left[ 1 + \frac{\ell_c^6 (1 - \gamma) (\lambda_\ell - \lambda_w) - \ell_c^3 \lambda_\ell}{4\ell_c^3 (1 - \gamma) - 2} + \mathcal{O}(\zeta^2) \right]. \end{aligned} \quad (41)$$

In real life, sessile droplets frequently take nonaxisymmetric shapes [7,8]. However, to the best of our knowledge, the range of length  $\ell$  and width  $w$  accessible to sessile droplets has not been systematically determined yet as a function of contact angle hysteresis.

When a cuboid drop starts at rest in a symmetric configuration different from equilibrium, i.e., with  $\ell_i = w_i \neq \ell_c$ , it relaxes towards an equilibrium solution within the range defined by contact angle hysteresis according to Eq. (40). The reached equilibrium position depends on initial conditions, as shown in Fig. 8 for the specific case  $\gamma = 0$ ,  $\text{Bo}_z = 0$ ,  $\text{Oh} = 0.1$ , and  $\zeta = 0.1$ .

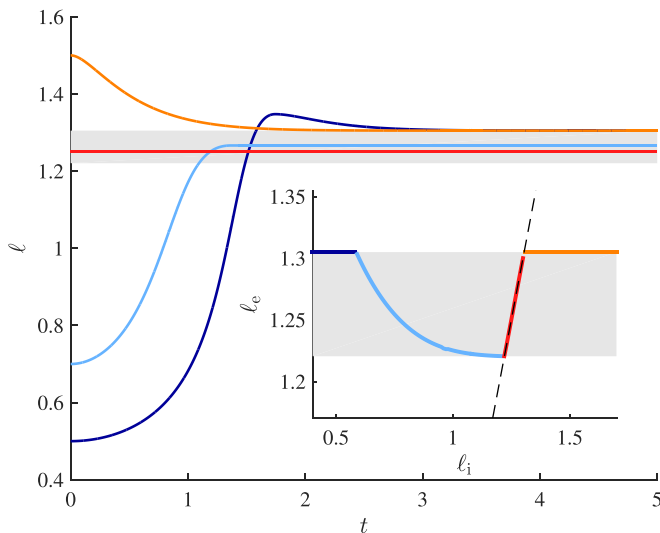


FIG. 8. Time evolution of the length  $\ell(t)$  of a symmetric cuboid drop ( $\ell = w$ ), for different initial conditions  $\ell_i$ , and parameters  $\gamma = 0$ ,  $\text{Bo}_z = 0$ ,  $\text{Oh} = 0.1$ , and  $\zeta = 0.1$ . (Inset) Reached equilibrium position  $\ell_e$  as a function of  $\ell_i$ . In both the main graph and the inset, the grey shading represents the region in which cuboid drops may remain static owing to hysteresis. In the inset, each color corresponds to trajectories that are qualitatively similar to the trajectory represented in the main graph. The dashed line is the bisector  $\ell_e = \ell_i$ .

With such relatively high dissipation, cuboid drops that are initially spread more than allowed by hysteresis (i.e.,  $\ell_i > 1.3$ ) retract monotonously until they reach the receding boundary ( $\lambda_\ell = -\zeta$ ). By contrast, cuboid drops that start from rest with a sufficiently oblong shape (namely, here with  $\ell_i < 0.58$ ) may still spread beyond the hysteresis region and subsequently retract (i.e., the contact line stops at the receding limit).

#### D. Retraction speed at different Oh

Bartolo *et al.* [38] provided extensive measurements of the maximal retraction rate experienced by drops after impact and spreading on a slightly hydrophilic substrate, for different water-glycerol mixtures (i.e., different Oh, cf. Fig. 9). We simulated the retraction of cuboid drops in the same conditions, starting from rest at maximal spreading  $\ell_i$ . The considered wetting parameters are  $\gamma = 0.17$  (contact angle  $\theta_r = 80^\circ$ ) and  $\zeta = 0.01$  [39]. The drop radius was experimentally varied between 1.1 and 1.4 mm, which corresponds to  $\text{Bo}_z \in [-0.72, -0.45]$ . For the simulations with cuboid drops, we consider  $\text{Bo}_z = -0.6$  and check that its influence on the following results is negligible. The maximum retraction speed is normalized by the capillary time and by the radius from which the drop starts retracting. In the simulations, it corresponds to  $\max_r(|\dot{\ell}|/\ell_i)$ . In the experiments, the diameter at initial spreading was in the range [6, 10] once normalized in the same way as  $\ell_i$ , so in the simulations, we consider both  $\ell_i = 6$  and  $\ell_i = 10$ .

The cuboid model predicts a maximum retraction rate that is qualitatively similar to that observed experimentally, and with the same order of magnitude (Fig. 9). Nevertheless, the dissipation seems systematically overestimated in the model (the predicted rate is lower than observed, for a given Oh), especially for large initial spreading  $\ell_i$ . This lower dissipation in experiments may result from the presence of a thick rim that is not captured by the model. It is mostly the fluid inside this rim that moves inward, and the corresponding dissipation is comparatively small because the rim thickness is larger than the corresponding cuboid thickness.

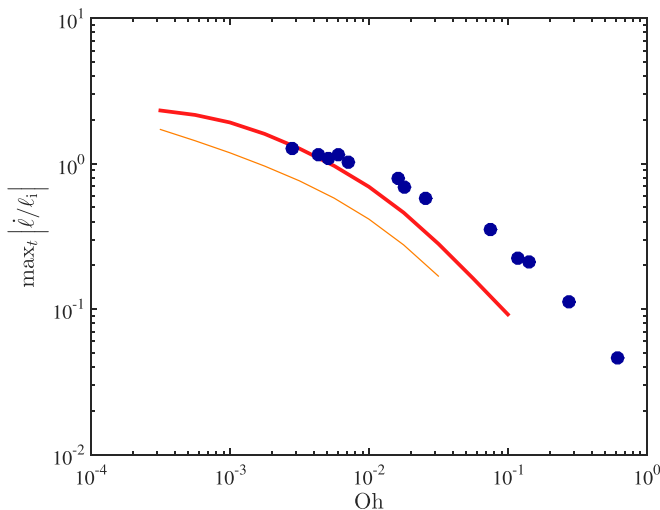


FIG. 9. Maximum retraction rate  $|\dot{\ell}/\ell_i|$  experienced by a sessile drop, as a function of Oh, for  $\text{Bo}_z = -0.6$ ,  $\gamma = 0.17$  and  $\zeta = 0.01$ . The dots correspond to measurements from Bartolo *et al.* [38] (with  $\text{Bo}_z \in [-0.72, -0.45]$  and initial normalized spreading diameter between 6 and 10). The thick red line (respectively, thin orange line) corresponds to numerical simulations of cuboid drops with  $\ell_i = 6$  (respectively,  $\ell_i = 10$ ).

### E. Sliding along $x$ at constant speed ( $\ddot{x}_G = 0$ ) and shape ( $\dot{\ell} = \dot{w} = 0$ )

Several experimental studies quantified the steady sliding of drops on inclined substrates. We compare the numerical predictions of the cuboid model to the measurements of Kim *et al.* [29], Podgorski *et al.* [40], Podgorski [41], and Le Grand *et al.* [42]. In the present model, the cuboid drop is assumed to slide in the direction of increasing  $x$ , so the contact line advances in B and recedes in A. Consequently, the forces at the contact line do not contribute to the dynamics of  $\ell$  (i.e.,  $\lambda_\ell = 0$ ), but they contribute to the dynamics of  $x_G$ , the corresponding force being  $-2\zeta w$ . In the width direction, the force per unit width at the contact line is still  $\lambda_w \ell$ , with  $\lambda_w \in [-\zeta, \zeta]$ . Under the assumption of sliding at constant speed  $\dot{x}_G$ , the Lagrange equation for  $x_G$  becomes

$$\frac{\partial \mathcal{E}}{\partial x_G} = -\frac{\partial \mathcal{D}}{\partial \dot{x}_G} - 2w\zeta \Rightarrow \text{Ca} = \frac{\text{Bo}_x - \text{Bo}_{xc}}{2I_3 \ell^2 w^2 + 2\Psi w}, \quad (42)$$

where  $\text{Ca} = \text{Oh}\dot{x}_G$  is the capillary number associated to the cuboid sliding speed, and  $\text{Bo}_{xc} = 2w\zeta$  is the critical Bond number (in the direction tangent to the substrate) at which the cuboid drop starts sliding. This critical Bond number corresponds to the body force that is required to oppose the capillary force at the contact lines in A and B.

Both the normalized sliding speed  $\text{Ca}$  and the critical bond number  $\text{Bo}_{xc}$  depend on  $w$ , which may take any value in a range prescribed by contact angle hysteresis, through Eq. (40) with  $\lambda_\ell = 0$  and  $\lambda_w \in [-\zeta, \zeta]$ . The corresponding range of  $\text{Ca}$  is shown in Fig. 10. Simulations with various initial cuboid drop shapes  $(\ell_i, w_i)$  converge to steady sliding within that range. The speed is maximal when the width is minimal, i.e., when  $\lambda_w = \zeta$  (advancing lateral contact line).

The normalized mobility of the drop, defined as  $\partial \text{Ca} / \partial \text{Bo}_x$ , is represented in Fig. 11. This parity plot compares the mobility predicted by the cuboid model Eq. (42) to the mobility inferred from sliding velocity measurements. The cuboid model correctly predicts the order of magnitude of the mobility of oil drops (experiments of Podgorski *et al.* [40], Podgorski [41], and Le Grand *et al.* [42]). However, it fails at reproducing the mobility measurements of Kim *et al.* [29], which are an order of magnitude lower than predicted. These measurements involved ethylene-glycol drops sliding on polycarbonate. Ethylene-glycol is a polar liquid with a molecular mass an order of magnitude lower

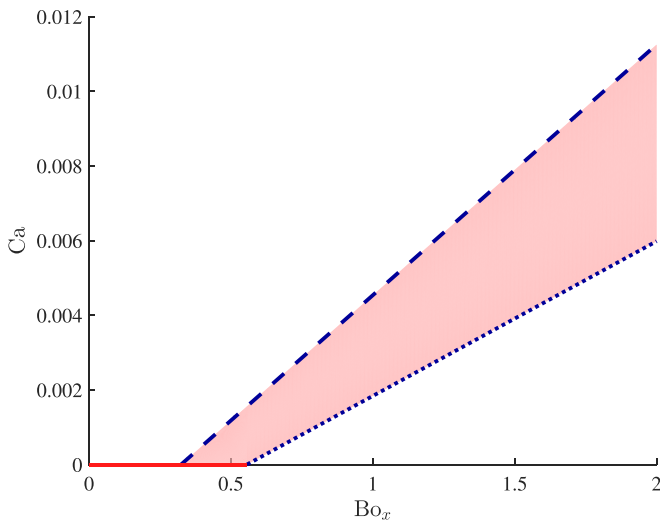


FIG. 10. Normalized speed  $Ca$  of a steadily sliding cuboid drop, as a function of the normalized body force  $Bo_x$  tangential to the substrate. The parameters are  $Bo_z = -2$ ,  $Oh = 0.02$ ,  $\gamma = 0.7$ , and  $\zeta = 0.1$ . The red shaded area (collapsed in red line at low  $Bo_x$ ) corresponds to different  $\lambda_w$  in steady state, that can be reached from different initial conditions  $(\ell_i, w_i)$ . The dashed (respectively, dotted) blue line represents equation (42) with  $\lambda_w = \zeta$  (respectively,  $\lambda_w = -\zeta$ ).

than the oils considered in the other experiments. Consequently, the slip length  $\Lambda$  should be smaller, and the factor  $\Psi$  involved in the viscous dissipation at the contact line [Eq. (15)] should be larger. Nevertheless, this expected increase of  $\Psi$  is estimated at 20%, so it cannot explain the observed discrepancy. We took additional measurements with ethylene-glycol drops on at the bottom of an

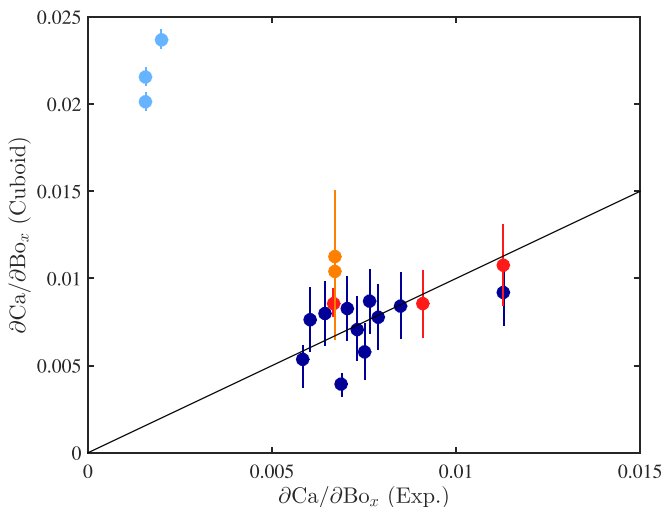


FIG. 11. Parity plot of the normalized mobility  $\partial Ca/\partial Bo_x$  for the cuboid drop vs experiments from Podgorski *et al.* [40] and Podgorski [41] (dark blue dots), Le Grand *et al.* [42] (red dots), Kim *et al.* [29] (light blue dots) and original measurements reported in the Supplemental Material [30] (orange dots). The error bars correspond to  $\lambda_w \in [-\zeta, \zeta]$  in the cuboid model [Eqs. (40) and (42)] and the dots are in  $\lambda_w = 0$ . The black line is the bisector of the first quadrant.

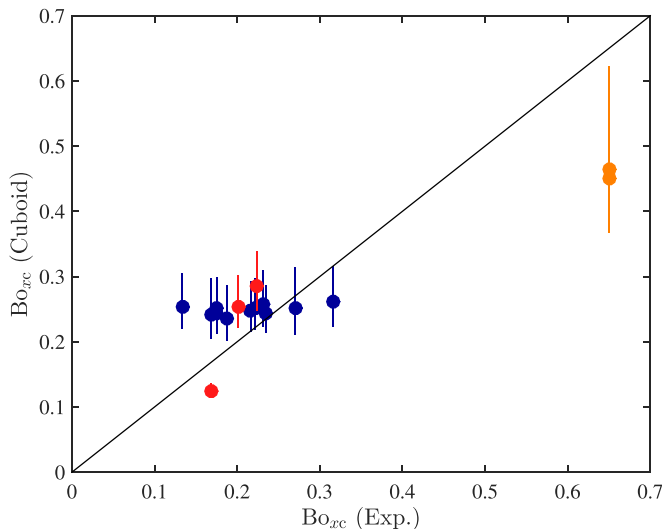


FIG. 12. Parity plot of the critical Bond number  $Bo_{xc}$  for the cuboid drop vs experiments from Podgorski *et al.* [40] and Podgorski [41] (dark blue dots), Le Grand *et al.* [42] (red dots), and original measurements reported in Supplemental Material [30] (orange dots). The error bars correspond to  $\lambda_w \in [-\zeta, \zeta]$  in the cuboid model [Eqs. (40) and (42)] and the dots are in  $\lambda_w = 0$ . The black line is the bisector of the first quadrant.

inclined polystyrene Petri dish (cf. Supplemental Material [30]). The cuboid prediction is much closer to these new mobility measurements.

The parity plot comparing cuboid predictions and drop measurements of the critical Bond number  $Bo_{xc}$  at the onset of sliding is represented in Fig. 12. Contact angle hysteresis was not reported in the experimental data from Kim *et al.* [29], so their data cannot be included. Again, the cuboid model predicts the correct order of magnitude, but fails at capturing the subtle variations of  $Bo_{xc}$  observed experimentally.

### F. Lateral motion upon forced substrate vibrations

Several experimental studies investigated drop motion on vibrated substrates (e.g., Noblin *et al.* [19], Costalonga and Brunet [43]). Among them, Brunet *et al.* [44] considered drops on an inclined substrate that is vibrated in the vertical direction. In a specific range of vibration amplitude and frequency, the drop may climb uphill instead of sliding downhill. The observed drop vibration involves a strong component of rocking mode that, by definition, cannot be captured by the cuboid model. Nevertheless, some climbing can be reproduced for the cuboid drop, that mostly involves the zonal, symmetric mode described in Sec. III B. The considered parameters are similar to those for which Brunet *et al.* [44] observed climbing. The drop volume was  $\Omega = 5 \mu\text{L}$ , and the liquid properties were  $\rho = 1190 \text{ kg/m}^3$ ,  $\mu = 36.9 \text{ cP}$ ,  $\sigma = 66 \text{ mN/m}$ ,  $\theta_a = 77^\circ$ , and  $\theta_r = 44^\circ$ . The corresponding surface energy ratio, hysteresis and Ohnesorge number are  $\gamma = 0.472$ ,  $\zeta = 0.25$  and  $Oh = 0.1$ , respectively. The substrate was inclined at  $45^\circ$  and vibrated with a frequency  $f = 30 \text{ Hz}$  and an acceleration amplitude  $a_s = 30$  (expressed in  $g$ ). This corresponds to a dimensionless frequency  $\omega_s = 2\pi f \sqrt{\rho\Omega/\sigma} = 1.79$  and Bond numbers  $Bo_x = Bo_z = (Bo/\sqrt{2})[a_s \sin(\omega_s t) - 1]$  with  $Bo = 0.517$ . A typical trajectory is represented in Fig. 13, and illustrated in Movie 3 available in the Supplemental Material [30]. The drop indeed moves upward on the substrate (increasing  $x_G$ ). We checked that the initial conditions do not significantly influence this steady climbing regime to which the drop converges. The capillary number corresponding to the time-averaged climbing speed  $\langle \dot{x}_G \rangle$  is  $Ca = Oh \langle \dot{x}_G \rangle \simeq 8.8 \times 10^{-3}$ , which is of the same order of magnitude as the capillary numbers observed in Brunet *et al.* [44].

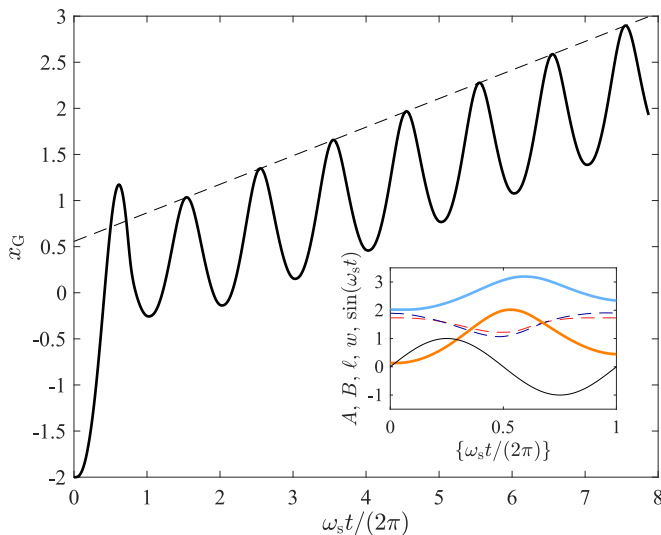


FIG. 13. Time evolution of the position  $x_G$  of the cuboid center of mass for parameters  $\gamma = 0.47$ ,  $\zeta = 0.25$ ,  $\text{Oh} = 0.1$ ,  $\omega_s = 1.79$ ,  $\text{Bo} = 0.517$ ,  $a_s = 30$ , and  $\text{Bo}_x = \text{Bo}_z = (\text{Bo}/\sqrt{2})[a_s \sin(\omega_s t) - 1]$ . The thick line represents  $x_G$  vs time normalized by the vibration period,  $\omega_s t / (2\pi)$ . The dashed line passes through the maxima of  $x_G$  (starting from the second) and corresponds to climbing at the time-averaged velocity  $\langle \dot{x}_G \rangle$  of the cuboid drop. (inset) Time evolution of the contact line A (thick orange line), the contact line B (thick light blue line), the cuboid length  $\ell$  (dashed dark blue line) and its width  $w$  (dashed red line) over one forcing period. The black line corresponds to  $\sin(\omega_s t)$ , which varies linearly with the forcing acceleration.

The motion of the cuboid drop during one forcing period is shown in the inset of Fig. 13. The drop vibration is essentially symmetric ( $w \simeq \ell$ ), which corresponds to the zonal mode. The drop moves downward and spreads (increasing  $\ell$  and  $w$ ) when the acceleration is downward ( $\sin \omega_s t < 0$ ), and it moves upward and recoils when the acceleration is upward. The contact line A is slightly in advance with respect to the contact line B over the whole forcing period, which is consistent with the observations of Brunet *et al.* [44] (although the phase shift is here significantly smaller than in Brunet *et al.* [44]).

Climbing cuboid drops are obtained for forcing parameters in the upper-left corner of the  $(\omega_s, a_s)$  phase space, i.e., for sufficiently small frequency and sufficiently large acceleration, consistently with the observations of Brunet *et al.* [44]. However, the region of climbing is significantly reduced for the cuboid drop, which may result from the absence of rocking mode. Significant sliding of the cuboid drop was also observed outside of the climbing zone, while in similar conditions, Brunet *et al.* [44] observed marginal sliding.

### G. Damping induced by a sessile drop on a vibrating cantilever beam

The last test case of this work is a configuration investigated experimentally by Erfanul Alam and Dickerson [45]: a drop was placed on a cantilever beam and the damping of this beam under natural vibrations was measured (Fig. 14). The drop also vibrated in response to the beam vibration, and contributed significantly to the damping. In first approximation, this contribution can be estimated from Erfanul Alam and Dickerson [45] by subtracting the measured decay rate induced by a beam without drop from decay-with-drop measurements.

In our lumped-element model of this experiment, the real drop is replaced by a cuboid drop and the beam is replaced by a proof mass supported by a linear spring (Fig. 14). The beam-induced damping is neglected. We consider only the mass and stiffness associated to the first mode of deformation (cf. Supplemental Material [30]). Other beam modes could be included, but it would

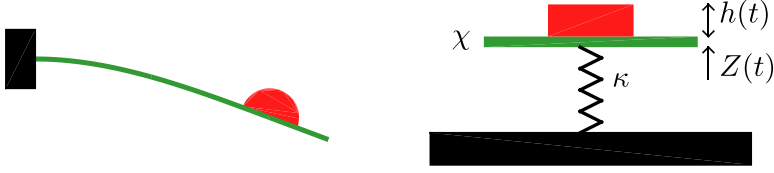


FIG. 14. Lumped-element model of the coupled vibration of a drop on a cantilever beam. (Left) The configuration investigated by Erfanul Alam and Dickerson [45]. (Right) The associated lumped-element model. The real drop is replaced by a cuboid drop of height  $h(t)$ . The beam is replaced by a rigid board (proof mass) of mass  $\chi$  at vertical position  $Z(t)$  supported by a spring of stiffness  $\kappa$ . All variables in the lumped-element model are dimensionless.

increase the number of variables in the Lagrangian, which limits the possibility to obtain insightful analytic results. We define the dimensionless proof mass  $\chi$  (normalized by drop mass  $\rho\Omega$ ) and the dimensionless spring stiffness  $\kappa$  (normalized by surface tension  $\sigma$ ). The observed drop vibration modes were mostly axisymmetric, so we may assume that the cuboid drop evolves with  $w = \ell$  at any time, i.e., only the zonal mode (2,0) is excited. Significant hysteresis was present in the experiments of Erfanul Alam and Dickerson [45], with  $\theta_a = 139^\circ$  and  $\theta_r = 119^\circ$ . Nevertheless, we neglect this hysteresis in the model ( $\gamma = -0.63$ ,  $\zeta = 0$ , no contact line pinning), again for the sake of finding an analytic solution. Erfanul Alam and Dickerson [45] did not observe significant lateral motion of the drop in response to the centrifugal force induced by the beam vibration. Consequently, we take  $\text{Bo}_x = \dot{x}_G = 0$ . Finally, the beams investigated in Erfanul Alam and Dickerson [45] experienced accelerations much higher than gravity (at least during the first part of the vibration), so we assume  $\text{Bo}_z \simeq 0$ .

We choose to describe the system with the generalized coordinates  $h(t)$  and  $Z(t)$ , the former being the cuboid thickness and the latter being the vertical position of the proof mass. Volume conservation of the cuboid drop implies  $h = 1/\ell^2$ . The potential energy of the system is

$$\mathcal{E} = 4h^{1/2} + (1 - \gamma)h^{-1} + \frac{\kappa Z^2}{2}. \quad (43)$$

The vertical fluid velocity is

$$u_z = F(\bar{z})\dot{h} + \dot{Z},$$

from which we deduce the kinetic energy of the system

$$\mathcal{K} = \left( \frac{I_1}{24h^3} + I_2 \right) \frac{\dot{h}^2}{2} + I_4 \dot{Z}^2 + (1 + \chi) \frac{\dot{Z}^2}{2}, \quad (44)$$

where

$$I_4 = \int_0^1 F(\bar{z}) d\bar{z} = 3/8 \quad (45)$$

for the considered shear function. The dissipation inside the cuboid drop,

$$\mathcal{D} = \text{Oh} \left( \frac{6I_1}{h^2} + \frac{I_3}{12h^5} + \frac{\Psi}{4h^{7/2}} \right) \frac{\dot{h}^2}{2}, \quad (46)$$

does not explicitly depend on the proof mass position  $Z$ . The resulting Lagrange equations are

$$(1 + \chi)\ddot{Z} + I_4\ddot{h} = -\kappa Z, \\ I_4\ddot{Z} + \left( \frac{I_1}{24h^3} + I_2 \right) \dot{h} = \frac{I_1\dot{h}^2}{16h^4} - 2h^{-1/2} + (1 - \gamma)h^{-2} - \text{Oh} \left( \frac{6I_1}{h^2} + \frac{I_3}{12h^5} + \frac{\Psi}{4h^{7/2}} \right) \dot{h}. \quad (47)$$

TABLE II. Asymptotic regimes of the two families of roots ( $s_1 = -\beta_1 \pm i\omega_1$  and  $s_2 = -\beta_2 \pm i\omega_2$ ) of the characteristic polynomial (52) describing the vibrations of the cuboid drop on mass-spring system, when either ( $\tilde{\text{Oh}} \ll 1$  and  $\tilde{\kappa} \ll 1$ ), ( $\tilde{\text{Oh}} \ll 1$  and  $\tilde{\kappa} \gg 1$ ), or ( $\tilde{\text{Oh}} \gg 1$ ).

$\tilde{\text{Oh}}$	$\ll 1$	$\ll 1$	$\gg 1$
$\tilde{\kappa}$	$\ll 1$	$\gg 1$	–
$\omega_1^2$	$\frac{1}{E_1} \tilde{\kappa}$	$E_2 \tilde{\kappa}$	$\frac{1}{E_1} \tilde{\kappa}$
$\beta_1$	$\frac{E_1 E_2 - 1}{2E_1^2} \tilde{\kappa}^2 \tilde{\text{Oh}}$	$\frac{E_1 E_2 - 1}{2E_2} \tilde{\text{Oh}}$	$\frac{E_1 E_2 - 1}{2E_1^2} \tilde{\kappa} \tilde{\text{Oh}}^{-1}$
$\omega_2^2$	$E_1$	$\frac{1}{E_2}$	0
$\beta_2$	$\frac{E_1}{2} \tilde{\text{Oh}}$	$\frac{1}{2E_2} \tilde{\text{Oh}}$	$\tilde{\text{Oh}}^{-1}, E_1 \tilde{\text{Oh}}$

We consider vibrations of small amplitude,  $h = \ell_0^{-2}(1 + \eta)$ ,  $|\eta| \ll 1$ . Consequently, the Lagrange equations can be linearized:

$$\begin{bmatrix} D_1 & D_2 \\ D_2 & D_3 \end{bmatrix} \begin{bmatrix} \ddot{Z} \\ \ddot{\eta} \end{bmatrix} + \text{Oh} \begin{bmatrix} 0 & 0 \\ 0 & D_4 \end{bmatrix} \begin{bmatrix} \dot{Z} \\ \dot{\eta} \end{bmatrix} + \begin{bmatrix} \kappa & 0 \\ 0 & D_5 \end{bmatrix} \begin{bmatrix} Z \\ \eta \end{bmatrix} = \begin{bmatrix} 0 \\ 0 \end{bmatrix}, \quad (48)$$

with

$$D_1 = 1 + \chi, \quad D_2 = \frac{I_4}{\ell_0^2}, \quad D_3 = \frac{I_1 \ell_0^2}{24} + \frac{I_2}{\ell_0^4}, \quad D_4 = 6I_1 + \frac{I_3 \ell_0^6}{12} + \frac{\Psi \ell_0^3}{4}, \quad \text{and} \quad D_5 = \frac{3}{\ell_0}. \quad (49)$$

Natural linear vibrations correspond to solutions  $Z = Z_i e^{st}$ ,  $\eta = \eta_i e^{st}$ , where  $s$  is a complex root of the fourth-order characteristic polynomial

$$(D_1 D_3 - D_2^2) s^4 + \text{Oh} D_1 D_4 s^3 + (\kappa D_3 + D_1 D_5) s^2 + \text{Oh} \kappa D_4 s + \kappa D_5 = 0. \quad (50)$$

The coefficient of  $s^4$ ,  $D_1 D_3 - D_2^2$ , is strictly positive since

$$\int_0^1 (F - I_4)^2 d\bar{z} = I_2 - I_4^2 > 0.$$

We define

$$E_1 = \frac{D_1 D_5}{D_1 D_3 - D_2^2}, \quad E_2 = \frac{D_3}{D_5}, \quad \tilde{\text{Oh}} = \frac{D_4}{D_5} \text{Oh}, \quad \tilde{\kappa} = \frac{D_5}{D_1 D_3 - D_2^2} \kappa, \quad (51)$$

so the polynomial can be rewritten as

$$s^4 + E_1 \tilde{\text{Oh}} s^3 + (E_1 + E_2 \tilde{\kappa}) s^2 + \tilde{\text{Oh}} \tilde{\kappa} s + \tilde{\kappa} = 0. \quad (52)$$

The roots  $s$  of the characteristic polynomial (52) can be written  $s = -\beta \pm i\omega$ , where  $\beta$  is the decay rate and  $\omega$  is the angular frequency. The decay rates associated to the different vibration modes are represented in Fig. 15, for the case  $\tilde{\kappa} \gg 1$ . Roots  $s$  can be obtained analytically in the asymptotic regimes associated to  $\tilde{\text{Oh}}$  and  $\tilde{\kappa}$ , as summarized in Table II. When  $\tilde{\text{Oh}} \ll 1$ , there are two sets of complex-conjugated roots. The first frequency  $\omega_1$  satisfies

$$\omega_1^2 = \frac{\tilde{\kappa}}{E_1} = \frac{\kappa}{1 + \chi} \quad (53)$$

when  $\tilde{\kappa} \ll 1$ , and

$$\omega_1^2 = E_2 \tilde{\kappa} = \frac{\kappa}{1 + \chi - \frac{I_4^2}{I_2 + \frac{I_4 \ell_0^6}{24}}} \quad (54)$$

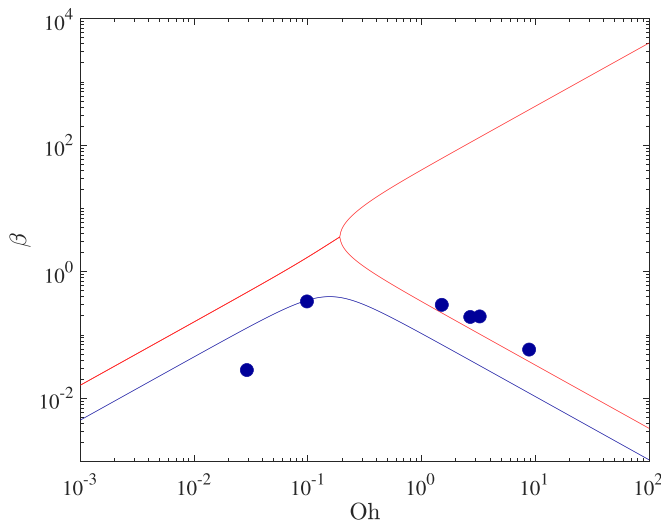


FIG. 15. Decay rates  $\beta_1$  (dark blue) and  $\beta_2$  (red) of the vibration modes associated to the cuboid drop on mass-spring system, as a function of the Ohnesorge number  $\text{Oh}$ , for  $\chi = 2.1$  and  $\kappa = 160$ . The solid lines correspond to the cuboid drop while the dark blue dots correspond to values inferred from the data of Erfanul Alam and Dickerson [45], for their beam of intermediate thickness. The corresponding asymptotic regimes are given in Table II.

when  $\tilde{\kappa} \gg 1$ . It essentially corresponds to the vibration of both proof mass and drop together as a rigid body, i.e., without drop deformations. The second frequency  $\omega_2$  satisfies

$$\omega_2^2 = E_1 = \frac{6\ell_0^{-3}}{\frac{l_1}{12} + \frac{2l_2}{\ell_0^6} - \frac{2l_3^2}{(1+\chi)\ell_0^6}} \quad (55)$$

when  $\tilde{\kappa} \ll 1$ , and

$$\omega_2^2 = \frac{1}{E_2} = \frac{6\ell_0^{-3}}{\frac{l_1}{12} + \frac{2l_2}{\ell_0^6}} \quad (56)$$

when  $\tilde{\kappa} \gg 1$ . It essentially corresponds to the symmetric deformation of the drop only, and it is highly similar to the vibration frequency of a cuboid drop on a fixed substrate, given by equation (38). When  $\tilde{\text{Oh}} \gg 1$ , the first set of roots  $s$  associated to the rigid body vibration at frequency  $\omega_1$  remains, while the two other roots, associated to the drop deformation, are now real (overdamped vibration), with decay rates  $\beta_2 \simeq \tilde{\text{Oh}}^{-1}$  or  $\beta_2 \simeq E_1 \tilde{\text{Oh}}$ .

The damping ratio  $\tilde{\beta} = \beta/\omega$  is proportional to  $\tilde{\text{Oh}}$  when  $\tilde{\text{Oh}} \ll 1$  and inversely proportional to  $\tilde{\text{Oh}}$  when  $\tilde{\text{Oh}} \gg 1$ . Consequently, there is a finite value of  $\tilde{\text{Oh}}$  that maximizes  $\tilde{\beta}$ :

$$\max_{\text{Oh}} \tilde{\beta} \simeq \begin{cases} \frac{E_1 E_2 - 1}{2E_1^2} \tilde{\kappa} & \text{in } \tilde{\text{Oh}} = E_1^{1/2} \tilde{\kappa}^{-1/2} & \text{when } \tilde{\kappa} \ll 1, \\ \frac{E_1 E_2 - 1}{2(E_1 E_2)^{3/4}} & \text{in } \tilde{\text{Oh}} = \left(\frac{E_2}{E_1}\right)^{3/4} \tilde{\kappa}^{1/2} & \text{when } \tilde{\kappa} \gg 1. \end{cases} \quad (57)$$

The damping ratio obtained for  $\tilde{\kappa} \gg 1$  corresponds to the maximum achievable damping ratio  $\tilde{\beta}$ . It increases with decreasing  $\chi$  and with decreasing  $\gamma$ . Consequently, the largest possible damping correspond to the limit  $\chi \rightarrow 0$  and  $\gamma \rightarrow -1$ , so to  $E_1 E_2 = \frac{l_1 + 24l_2}{l_1 + 24(l_2 - l_3^2)} \simeq 1.97$  and it yields  $\tilde{\beta} \simeq 0.29$ .

The decay rate inferred from the experiments of Erfanul Alam and Dickerson [45] is compared to the cuboid prediction in Fig. 15. Both modes are excited in experiments (cf. videos online in

Ref. [45]), with unknown initial amplitudes, so the measured decay rate should be a combination of the rates of each mode. This may explain why the dots of Fig. 15 are not preferentially captured by either theoretical curve. Nevertheless, the predicted decay rate is in qualitative agreement with the corresponding measurements: it is of the same order of magnitude, and its nonmonotonous dependence on Oh is retrieved.

#### IV. CONCLUSION

In this paper, we introduced a low-dimensional model of the dynamics of a drop on a substrate. The drop shape was approximated by a rectangular cuboid. This shape was sufficiently simple to allow closed-form expressions of the potential and kinetic energy, and the viscous dissipation (in bulk and at contact lines). The time evolution of the position and dimensions of the cuboid drop was given by the corresponding Lagrange equations, thereby ensuring momentum balance at drop scale even though the chosen velocity profile did not satisfy Navier-Stokes equations. Contact angle hysteresis was included as an additional force that was adjusted in a finite range to possibly constraint the contact line position (pinning). The model yielded a system of three ordinary differential equations that could be solved numerically to predict the motion and deformation of the drop in response to time-varying external forces.

Many closed-form solutions to the Lagrange equations could be found, in steady states or for small perturbations (linearized equations). In particular, analytic expressions could be obtained to describe the stability limit of pendant drops, the first zonal and sectoral vibration modes, and the sliding of drops at constant speed.

Existing low-dimensional models of drops [18,19], mostly based on a proof mass and one or several linear springs, could already capture the dynamical coupling between drop position and drop deformation (e.g., during bouncing, or in response to substrate vibrations). By comparison, the cuboid model offers additional capabilities: it qualitatively captures, e.g., the instability of drops pulled away from the substrate, the history-dependent shape of drops in the presence of contact angle hysteresis, or the nonlinear retraction of drops after large spreading. Surprisingly, it could also reproduce the climbing of drops on vibrated inclined substrates [44], though not in a range of parameters as extended as observed experimentally. This discrepancy is likely due to the lack of rocking mode in the rectangular cuboid approximation. Other modes, absent in this rectangular cuboid, would also have to be considered to model specific drop-substrate interactions, e.g., the rolling mode associated to drop motion parallel to the substrate [46].

An extension of the model to more general shapes with additional degrees of freedom would possibly allow to capture these missing modes, including rocking or rolling. Such extension is left to future work. Necessarily, the more freedom is given to the drop shape, the less likely closed-form solutions are to be found for the elementary cases considered in this study. In the same direction, in an exact model of a sessile drop, the interface shape would have an infinite number of degrees of freedom, the velocity profile would be obtained from Navier-Stokes equations, and the corresponding pressure field would satisfy the Young-Laplace equation at the liquid-air interface.

Finally, we demonstrated that the cuboid model can be easily coupled to other lumped elements. In particular, the cuboid drop could be placed on a proof-mass connected to a spring, to model the vibrations of a drop on a cantilever beam [45]. The adaptation only required a slight modification of the Lagrangian to include the energy associated to the motion of the proof-mass. Closed-form expressions for the decay rate of natural vibrations could be inferred in asymptotic regimes, and the parameters that maximize damping could be identified analytically.

The detachment of drops from the substrate was only considered in the static case of a pendant drop. Nevertheless, drops are expected to either break up or fully detach from the substrate in a variety of other conditions, including when bouncing at low Weber number [47]. Determining the criterion on cuboid shape that best captures the moment of drop detachment or breakup requires a thorough comparison to the large amount of literature on contact time at impact [22,48–52] and

is left to future work. Nevertheless, it is hoped that with such criterion, the model will be able to reproduce the main features of low-Weber drop impacts, including on flexible substrates [53–56].

In conclusion, this work introduced the cuboid drop as a low-dimensional model of drops on substrates. It predicts relevant orders of magnitude and qualitatively captures the dependence on parameters in a variety of classical configurations (vibrations, sliding, etc.). Moreover, it can reproduce some complex dynamics of drops on moving substrates. This cuboid model has likely the appropriate level of complexity to run low-cost simulations of numerous interacting drops on a substrate, after minor adaptations to allow drop merger and breakup.

#### ACKNOWLEDGMENT

This work has been supported by the FNRS (Fond de la Recherche Scientifique) through the research grant J.0071.23 (Rainfall interception by plant leaves).

- 
- [1] S. R. Herwitz, Raindrop impact and water flow on the vegetative surfaces of trees and the effects on stemflow and throughfall generation, *Earth Surf. Processes Landforms* **12**, 425 (1987).
  - [2] C. D. Holder, The relationship between leaf water repellency and leaf traits in three distinct biogeographical regions, *Plant Ecol.* **212**, 1913 (2011).
  - [3] T. Gilet and L. Bourouiba, Rain-induced ejection of pathogens from leaves: Revisiting the hypothesis of splash-on-film using high-speed visualization, *Integr. Comp. Biol.* **54**, 974 (2014).
  - [4] A. Klamerus-Iwan, E. Blonska, J. Lasota, P. Waligorski, and A. Kalandyk, Seasonal variability of leaf water capacity and wettability under the influence of pollution in different city zones, *Atmos. Pollut. Res.* **9**, 455 (2018).
  - [5] J. André, C. Brochet, Q. Louis, A. Barral, A. Guillen, F.-T. Goh, A. Pietro, and T. Guillet, Motion of rain drops on a car side window, *Emergent Sci.* **3**, 3 (2019).
  - [6] F. Yu, J. Yang, R. Tao, Y. Tan, J. Wang, D. Wang, L. Chen, Z. Wang, and X. Deng, Aerodynamic super-repellent surfaces, *Research* **6**, 0111 (2023).
  - [7] G. Mc Hale, H. Y. Erbil, M. I. Newton, and S. Natterer, Analysis of shape distortions in sessile drops, *Langmuir* **17**, 6995 (2001).
  - [8] B. R. Prabhala, M. V. Panchagnula, and S. Vedantam, Three-dimensional equilibrium shapes of drops on hysteretic surfaces, *Colloid Polym. Sci.* **291**, 279 (2013).
  - [9] D. Nezlobin, H. Rubin, H. Lavee, P. Sarah, and E. Sachs, Runoff initiation from raindrops falling onto planar inclined surface, *Exp. Therm. Fluid Sci.* **46**, 8 (2013).
  - [10] T. Gilet and L. Bourouiba, Fluid fragmentation shapes rain-induced foliar disease transmission, *J. R. Soc. Interface* **12**, 20141092 (2015).
  - [11] M. D. Erfanul Alam, J. L. Kauffman, and A. K. Dickerson, Drop ejection from vibrating damped, dampened wings, *Soft Matter* **16**, 1931 (2020).
  - [12] Y. I. Frenkel, On the behavior of liquid drops on a solid surface: 1. The sliding of drops on an inclined surface, *J. Exp. Theor. Phys.* **18**, 658 (1948).
  - [13] A. I. ElSherbini and A. M. Jacobi, Liquid drops on vertical and inclined surfaces II. A method for approximating drop shapes, *J. Colloid Interface Sci.* **273**, 566 (2004).
  - [14] S. P. Thampi and R. Govindarajan, Minimum energy shapes of one-side-pinned static drops on inclined surfaces, *Phys. Rev. E* **84**, 046304 (2011).
  - [15] C. Semprebon and M. Brinkmann, On the onset of motion of sliding drops, *Soft Matter* **10**, 3325 (2014).
  - [16] J. B. Dupont and D. Legendre, Numerical simulation of static and sliding drop with contact angle hysteresis, *J. Comput. Phys.* **229**, 2453 (2010).
  - [17] L. C. Mayo, S. W. McCue, T. J. Moroney, W. Alison Foster, D. M. Kempthorne, J. A. Belward, and I. W. Turner, Simulating droplet motion on virtual leaf surfaces, *R. Soc. Open Sci.* **2**, 140528 (2015).

- [18] K. Okumura, F. Chevy, D. Richard, D. Quere, and C. Clanet, Water spring: a model for bouncing drops, *Europhys. Lett.* **62**, 237 (2003).
- [19] X. Noblin, R. Kofman, and F. Celestini, Ratchetlike motion of a shaken drop, *Phys. Rev. Lett.* **102**, 194504 (2009).
- [20] D. Terwagne, F. Ludewig, N. Vandewalle, and S. Dorbolo, The role of the droplet deformations in the bouncing, *Phys. Fluids* **25**, 122101 (2013).
- [21] T. M. Schutzius, S. Jung, T. Maitra, G. Graeber, M. Köhme, and D. Poulikakos, Spontaneous droplet trampolining on rigid superhydrophobic surfaces, *Nature (London)* **527**, 82 (2015).
- [22] J. Moláček and J. W. M. Bush, A quasi-static model of drop impact, *Phys. Fluids* **24**, 127103 (2012).
- [23] J. H. Moon, B. H. Kang, and H.-Y. Kim, The lowest oscillation mode of a pendant drop, *Phys. Fluids* **18**, 021702 (2006).
- [24] A. D. Myshkis, V. G. Babskii, N. D. Kopachevskii, L. A. Slobozhanin, and A. D. Tyuptsov, *Low-Gravity Fluid Mechanics: Mathematical Theory of Capillary Phenomena* (Springer-Verlag, Berlin, Heidelberg, 1987).
- [25] D. Richard and D. Quéré, Viscous drops rolling on a tilted non-wettable solid, *Europhys. Lett.* **48**, 286 (1999).
- [26] H.-J. Butt, J. Liu, K. Koynov, B. Straub, C. Hinduja, I. Roismann, R. Berger, X. Li, D. Vollmer, W. Steffen, and M. Kappl, Contact angle hysteresis, *Curr. Opin. Colloid Interface Sci.* **59**, 101574 (2022).
- [27] C. Huh and L. E. Scriven, Hydrodynamic model of steady movement of a solid/liquid/fluid contact line, *J. Colloid Interface Sci.* **35**, 85 (1971).
- [28] P.-G. de Gennes, Wetting: statics and dynamics, *Rev. Mod. Phys.* **57**, 827 (1985).
- [29] H.-Y. Kim, H. J. Lee, and B. H. Kang, Sliding of liquid drops down an inclined solid surface, *J. Colloid Interface Sci.* **247**, 372 (2002).
- [30] See Supplemental Material at <http://link.aps.org/supplemental/10.1103/PhysRevFluids.9.043601> for additional information.
- [31] The Lagrange equation describing the evolution of  $x_G$  is decoupled from the equations governing  $\ell$  and  $w$ . Moreover, there is no restoring force on  $x_G$ , suggesting that any perturbation is necessarily marginally stable in this direction. Consequently, perturbations along  $x_G$  are not considered.
- [32] C. Pozrikidis, Stability of sessile and pendant liquid drops, *J. Eng. Math.* **72**, 1 (2012).
- [33] J. B. Bostwick and P. H. Steen, Dynamics of sessile drops. Part 1. Inviscid theory, *J. Fluid Mech.* **760**, 5 (2014).
- [34] P. H. Steen, C.-T. Chang, and J. B. Bostwick, Droplet motions fill a periodic table, *Proc. Natl. Acad. Sci. USA* **116**, 4849 (2019).
- [35] F. Zhang, X. Zhou, and H. Ding, Effects of gravity on natural oscillations of sessile drops, *J. Fluid Mech.* **962**, A10 (2023).
- [36] S. Mettu and M. K. Chaudhury, Vibration spectroscopy of a sessile drop and its contact line, *Langmuir* **28**, 14100 (2012).
- [37] Most experimental investigations of sessile drop vibrations (e.g., Moon *et al.* [23]) involved substrates with significant hysteresis. Therefore, for vibrations of small amplitude, contact angle variations remained smaller than contact angle hysteresis, and the contact lines remained pinned. These pinned vibrations cannot be reproduced by the present cuboid model.
- [38] D. Bartolo, C. Josserand, and D. Bonn, Retraction dynamics of aqueous drops upon impact on non-wetting surfaces, *J. Fluid Mech.* **545**, 329 (2005).
- [39] The hysteresis was not measured in Bartolo *et al.* [38], but it was claimed to be very weak.
- [40] T. Podgorski, J.-M. Flesselles, and L. Limat, Corners, cusps and pearls in running drops, *Phys. Rev. Lett.* **87**, 036102 (2001).
- [41] T. Podgorski, Ruissellement en conditions de mouillage partiel, Ph.D. thesis, Université Pierre et Marie Curie, 2003.
- [42] N. Le Grand, A. Daerr, and L. Limat, Shape and motion of drops sliding down an inclined plane, *J. Fluid Mech.* **541**, 293 (2005).
- [43] M. Costalonga and P. Brunet, Directional motion of vibrated sessile drops: A quantitative study, *Phys. Rev. Fluids* **5**, 023601 (2020).

- [44] P. Brunet, J. Eggers, and R. D. Deegan, Vibration-induced climbing of drops, [Phys. Rev. Lett. \*\*99\*\*, 144501 \(2007\)](#).
- [45] M. D. Erfanul Alam and A. K. Dickerson, Sessile liquid drops damp vibrating structures, [Phys. Fluids \*\*33\*\*, 062113 \(2021\)](#).
- [46] J. Xie, J. Xu, W. Shang, and K. Zhang, Mode selection between sliding and rolling for droplet on inclined surface: Effect of surface wettability, [Int. J. Heat Mass Transfer \*\*122\*\*, 45 \(2018\)](#).
- [47] C. Antonini, F. Villa, I. Bernagozzi, A. Amirfazli, and M. Marengo, Drop rebound after impact: The role of the receding contact angle, [Langmuir \*\*29\*\*, 16045 \(2013\)](#).
- [48] D. Richard, C. Clanet, and D. Quéré, Contact time of a bouncing drop, [Nature \(London\) \*\*417\*\*, 811 \(2002\)](#).
- [49] J. C. Bird, R. Dhiman, H.-M. Kwon, and K. K. Varanasi, Reducing the contact time of a bouncing drop, [Nature \(London\) \*\*503\*\*, 385 \(2013\)](#).
- [50] C. Antonini, F. Villa, and M. Marengo, Oblique impacts of water drops onto hydrophobic and superhydrophobic surfaces: Outcomes, timing, and rebound maps, [Exp. Fluids \*\*55\*\*, 1713 \(2014\)](#).
- [51] Y. H. Yeong, J. Burton, E. Loth, and I. S. Bayer, Drop impact and rebound dynamics on an inclined superhydrophobic surface, [Langmuir \*\*30\*\*, 12027 \(2014\)](#).
- [52] S. Yun and G. Lim, Ellipsoidal drop impact on a solid surface for rebound suppression, [J. Fluid Mech. \*\*752\*\*, 266 \(2014\)](#).
- [53] P. B. Weisensee, J. Ma, Y. H. Shin, J. Tian, Y. Chang, W. P. King, and N. Miljkovic, Droplet impact on vibrating superhydrophobic surfaces, [Phys. Rev. Fluids \*\*2\*\*, 103601 \(2017\)](#).
- [54] J.-H. Kim, J. P. Rothstein, and J. K. Shang, Dynamics of a flexible superhydrophobic surface during a drop impact, [Phys. Fluids \*\*30\*\*, 072102 \(2018\)](#).
- [55] X. Huang, X. Dong, J. Li, and J. Liu, Droplet impact induced large deflection of a cantilever, [Phys. Fluids \*\*31\*\*, 062106 \(2019\)](#).
- [56] G. Upadhyay, V. Kumar, and R. Bhardwaj, Bouncing droplets on an elastic, superhydrophobic cantilever beam, [Phys. Fluids \*\*33\*\*, 042104 \(2021\)](#).